

# A phenazine-based high-capacity and high-stability electrochemical CO<sub>2</sub> capture cell with coupled electricity storage

Received: 19 August 2022

Accepted: 2 August 2023

Published online: 24 August 2023



Shuai Pang<sup>1,2,7</sup>, Shijian Jin<sup>3,7</sup>, Fengcun Yang<sup>4</sup>, Maia Alberts<sup>5</sup>, Lu Li<sup>1,2</sup>, Dawei Xi<sup>3</sup>, Roy G. Gordon<sup>3,6</sup>, Pan Wang<sup>1,2</sup>✉, Michael J. Aziz<sup>3</sup>✉ & Yunlong Ji<sup>4</sup>✉

Carbon dioxide capture technologies will be important for counteracting difficult-to-abate greenhouse gas emissions if humanity is to limit global warming to acceptable levels. Electrochemically mediated CO<sub>2</sub> capture has emerged as a promising alternative to conventional amine scrubbing, offering a potentially cost effective, environmentally friendly and energy efficient approach. Here we report an electrochemical cell for CO<sub>2</sub> capture based on pH swing cycles driven through proton-coupled electron transfer of a developed phenazine derivative, 2,2'-(phenazine-1,8-diyl)bis(ethane-1-sulfonate) (1,8-ESP), with high aqueous solubility (>1.35 M) over pH range 0.00–14.90. The system operates with a high capture capacity of 0.86–1.41 mol l<sup>-1</sup>, a low energetic cost of 36–55 kJ mol<sup>-1</sup> and an extremely low capacity fade rate of <0.01% per day, depending on organic concentration. The system charge–discharge cycle provides an electrical energy storage function that could be run only for storage when called for by electricity market conditions.

The global average temperature today is more than 1 °C warmer compared to the pre-Industrial Revolution time<sup>1</sup>. Greenhouse gas emissions are the primary driver for climate change, where the accumulated CO<sub>2</sub> emissions from fossil fuel consumption are the major source and lead to global warming, ocean acidification and other severe environmental problems<sup>2,3</sup>. In addition to the rapid displacement of fossil energy by clean energy<sup>4</sup>, CO<sub>2</sub> capture, whether from a point source such as a fossil fuel or biomass combustion power plant<sup>5–7</sup> or directly from air<sup>8,9</sup>, is important because fossil fuel combustion is going to remain significant for a long time, and hard-to-abate emissions will still exist even if the electricity sector is fully decarbonized. To keep the global temperature rise under 1.5 °C by 2100, important progress needs to be achieved in efficient large-scale CO<sub>2</sub> capture techniques<sup>10</sup>.

Considerable research and development efforts have been made to develop CO<sub>2</sub> capture methods with low energy consumption, fast capture rate and high capture capacity (mol<sub>CO<sub>2</sub></sub> per litre of solvent)<sup>11–16</sup>. Amine scrubbing has been utilized at an industrial scale for post-combustion CO<sub>2</sub> capture from point sources<sup>11</sup>. Whereas the energy cost of amine scrubbing can be low, that is ~80 kJ mol<sub>CO<sub>2</sub></sub><sup>-1</sup> for advanced solvent systems, serious problems including material degradation, toxicity and corrosivity are concerning<sup>12</sup>. Electrochemically mediated CO<sub>2</sub> capture may provide a lower-cost, more environmentally benign and less energy-intensive approach that could be operated at ambient temperature and pressure without relying on external thermal energy<sup>17–20</sup>. CO<sub>2</sub> capture based on electrochemically induced pH swing, where CO<sub>2</sub> can be absorbed at high pH and released at low pH, is a promising

<sup>1</sup>Key Laboratory of Precise Synthesis of Functional Molecules of Zhejiang Province, Department of Chemistry, School of Science and Research Center for Industries of the Future, Westlake University, Hangzhou, China. <sup>2</sup>Institute of Natural Sciences, Westlake Institute for Advanced Study, Hangzhou, China. <sup>3</sup>John A. Paulson School of Engineering and Applied Sciences, Harvard University, Cambridge, MA, USA. <sup>4</sup>School of Chemistry and Materials Science, Hangzhou Institute for Advanced Study, University of Chinese Academy of Sciences, Hangzhou, China. <sup>5</sup>Harvard College, Cambridge, MA, USA. <sup>6</sup>Department of Chemistry and Chemical Biology, Harvard University, Cambridge, MA, USA. <sup>7</sup>These authors contributed equally: Shuai Pang, Shijian Jin. ✉e-mail: [wangpan@westlake.edu.cn](mailto:wangpan@westlake.edu.cn); [maziz@harvard.edu](mailto:maziz@harvard.edu); [jijunlong@ucas.ac.cn](mailto:jijunlong@ucas.ac.cn)

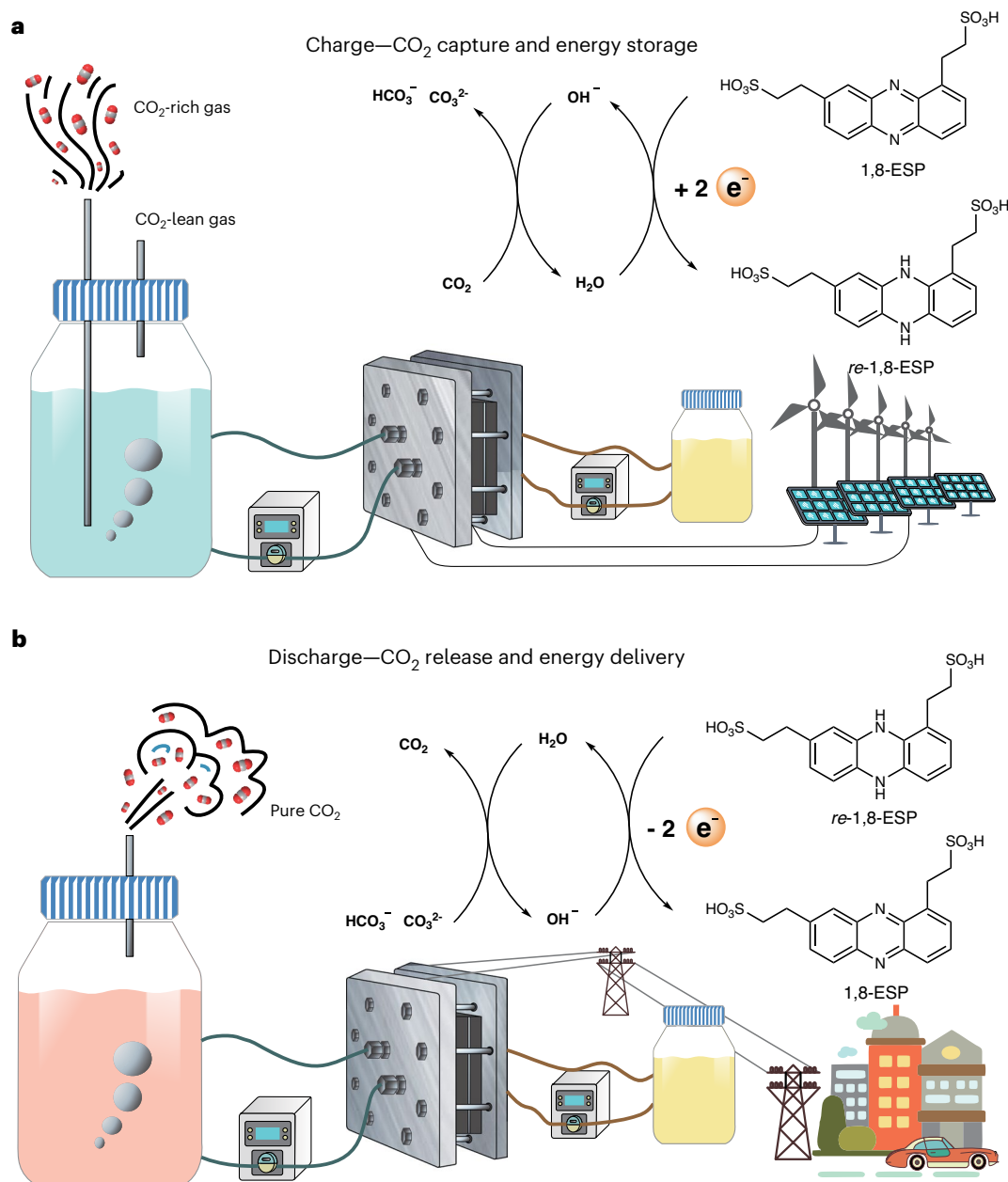


**Fig. 1 | Illustration of CO<sub>2</sub> capture–release and energy storage–delivery cycle associated with the cell charge and discharge process. **a**, CO<sub>2</sub> capture and energy storage process. **b**, CO<sub>2</sub> release and energy delivery process. *re*-1,8-ESP is the reduced state of 1,8-ESP.**

electrochemical carbon capture method because of its low energetic cost and high applicable current density<sup>21</sup>. Such a pH swing can be driven electrochemically through proton-coupled electron transfer (PCET) of organic molecules, that is, upon electrochemical reduction and oxidation, the molecules undergoing PCET reactions uptake and release protons, leading to pH decrease and increase, respectively, in the aqueous solution<sup>22–26</sup>. Leveraging the high tunability of redox-active organic molecules, electrolytes with desirable redox potential, high solubility, long lifetime and low cost may be realized<sup>27</sup>. Recently a proof-of-concept point source (10%) CO<sub>2</sub> separation system based on 3,3'-(phenazine-2,3-diyl)bis(oxo))bis(propane-1-sulfonate) (DSPZ) as the PCET carrier was shown to require a low energy cost of 61 kJ mol<sub>CO<sub>2</sub></sub><sup>−1</sup> at 20 mA cm<sup>−2</sup>, and results extrapolated to 121 kJ mol<sub>CO<sub>2</sub></sub><sup>−1</sup> for 0.4 mbar capture<sup>22,23</sup>. Nevertheless, the development of PCET molecules with improved aqueous solubility is necessary to enhance the CO<sub>2</sub> capture

capacity. Additionally, although various electrochemical CO<sub>2</sub> capture methods are reported, few have investigated the operational lifetime and stability of CO<sub>2</sub> capture materials<sup>28,29</sup>.

Here we report a high-capacity and high-stability electrochemical CO<sub>2</sub> capture system with coupled electricity storage. This system, based on an aqueous flow cell, employs the developed molecule sodium 2,2'-(phenazine-1,8-diyl)bis(ethane-1-sulfonate) (1,8-ESP) that exhibits remarkable redox activity and high solubility in any pH from acid to base, making it ideal as an agent to induce pH swing for CO<sub>2</sub> capture. The results of a detailed investigation of CO<sub>2</sub> capture capacity, energetic cost, capture rate and stability for electrolytes with 1,8-ESP at different concentrations are presented. 1,8-ESP cell demonstrates advantageous properties for both carbon capture and energy storage applications. Figure 1 shows a schematic illustration of the integrated CO<sub>2</sub> capture–release and energy storage–delivery system with 1,8-ESP.

In the charging process paired with ferrocyanide on the positive side (Fig. 1a), the pH and total alkalinity (TA) in solution increase (deacidification), and the CO<sub>2</sub>-containing gas reacts with OH<sup>-</sup> to form dissolved inorganic carbon (DIC), completing the CO<sub>2</sub> absorption and energy storage half cycle. During discharging (Fig. 1b), the pH and TA of the electrolyte decrease (acidification), resulting in pure CO<sub>2</sub> outgassing. During this half cycle, electrical energy delivery and pure CO<sub>2</sub> gas release occur simultaneously. Thus the capital requirements could be shared without further cost investments while concurrently providing storage services for the electrical grid, which must deal with increasing contributions from intermittent renewable power sources. Electricity price arbitrage in an electricity market is profitable only a small fraction of the time<sup>30</sup>; hence the dedication of the integrated system to CO<sub>2</sub> capture during periods when arbitrage is unprofitable could lead to significantly improved economics over those of comparable systems for either application alone.

## Electrochemical and physico-chemical studies of 1,8-ESP

ESP isomers with substituents at different positions of the phenazine core (1,8-ESP, 2,7-ESP, 1,6-ESP) were synthesized (Supplementary Note 1) and characterized by nuclear magnetic resonance (NMR; Supplementary Figs. 1–6) and high-resolution mass spectrometry. The solubilities of these isomers (Supplementary Figs. 7–13 and Supplementary Table 1) were studied by UV–vis spectroscopy analysis. The unsymmetrically substituted 1,8-ESP exhibits higher solubility than symmetrically substituted 2,7-ESP and 1,6-ESP; this shows the same trend as the theoretical study of solvation energies through density functional theory (DFT) calculations (Supplementary Tables 2 and 3). Thus we set out to investigate 1,8-ESP further for use as a CO<sub>2</sub> capture agent due to its high solubility, which enables high volumetric CO<sub>2</sub> capture capacity. 1,8-ESP exhibits a solubility of 1.40 M in 1.0 M KCl, corresponding to a theoretical CO<sub>2</sub> separation capacity ( $\Delta\text{DIC}_{3\rightarrow 1}$ )<sup>23</sup> of 2.35 mol<sub>CO<sub>2</sub></sub> l<sup>-1</sup> and 1.48 mol<sub>CO<sub>2</sub></sub> l<sup>-1</sup> at inlet CO<sub>2</sub> partial pressures of 100 mbar and 0.4 mbar CO<sub>2</sub>(g), which are the CO<sub>2</sub> concentration of flue gas from a typical coal power plant and atmospheric CO<sub>2</sub>, respectively. This high solubility (1.40 M) also means a theoretical negolyte volumetric capacity of 75.0 Ah l<sup>-1</sup> for energy storage. Assuming an equally concentrated, two-electron transfer couple in the counter-electrolyte, the cell volumetric capacity would be 37.5 Ah l<sup>-1</sup>. Besides being soluble in a pH-neutral solution, 1,8-ESP shows an even higher solubility of 1.60 M in 1.0 M H<sub>2</sub>SO<sub>4</sub>, 1.95 M in 1.0 M KOH and 2.06 M in 2.0 M KOH, minimizing the possibility of precipitation during the pH swing for CO<sub>2</sub> capture (Fig. 2a and Table 1). The solubility of 1,8-ESP is also explored in the presence of DIC. In a solution of 1.0 M TA that is saturated with 0.4 mbar CO<sub>2</sub> in air, that is, 0.436 M K<sub>2</sub>CO<sub>3</sub> and 0.128 M KHCO<sub>3</sub>, 1,8-ESP remains highly soluble (1.35 M), indicating its compatibility with DIC.

1,8-ESP possesses quasi-reversible redox electrochemical properties in a wide range of pH buffer solutions through cyclic voltammetry (CV) studies (Fig. 2b and Supplementary Fig. 14). As shown in the Pourbaix diagram of 1,8-ESP (Fig. 2c), the linear relationship between pH and potential, with a slope of  $-58.1 \text{ mV pH}^{-1}$  suggests that the molecule undergoes a two-proton/two-electron process in the pH frame within the experiment. Note that 1,8-ESP participates in  $\text{2H}^+$ ,  $2\text{e}^-$  PCET up to at least pH 14.90, suggesting a high capacity for CO<sub>2</sub> capture. To evaluate its redox reaction kinetics in solutions with different electrolytes, rotating disk electrode (RDE) experiments were carried out to analyse its diffusion coefficient (*D*) and electron transfer-rate constant (*k*<sub>0</sub>) (Supplementary Figs. 15–20). The calculated diffusion coefficients and electron transfer-rate constants according to the Tafel plots are reported in Table 1.

1,8-ESP has an extremely low permeability of  $1.24 \times 10^{-15} \text{ cm}^2 \text{ s}^{-1}$  across a cation-exchange membrane (Nafion NC700), suggesting a negligible crossover rate during cell operation (Supplementary Fig. 21). We attribute this to the large molecular structure and the deprotonated

sulfonic acids with negative charges (Supplementary Fig. 22) that repel 1,8-ESP molecules from the negatively charged membrane surface<sup>31,32</sup>. A key attribute sought in CO<sub>2</sub> absorption solution is a high surface tension, which helps to decrease foaming, commonly encountered in electrochemically mediated carbon capture<sup>33,34</sup>. 1,8-ESP solution has a higher surface tension than water, reducing foaming during cycling (Fig. 2d and Supplementary Figs. 23 and 24). Compared to the previously reported molecule DSPZ, 1,8-ESP exhibits a higher solubility and less foaming in solution, making it more attractive for electrochemical CO<sub>2</sub> separation.

## CO<sub>2</sub> capture cells and the energetic cost evaluation

Next we explored the energetic cost of the CO<sub>2</sub> absorption/release cycle. Figure 2e shows the schematic of the carbon capture flow cell and the hardware for providing the gas mixture and analysing the exhaust. The upstream gas composition in the negolyte headspace was controlled by CO<sub>2</sub> and N<sub>2</sub> mass flow controllers). Downstream of the negolyte reservoir, the gas was dried with a desiccator (Supplementary Fig. 25), and the total gas flow rate and CO<sub>2</sub> partial pressure were measured using a digital flow meter and a CO<sub>2</sub> sensor, respectively. A pH probe immersed in the negolyte solution reported the temporal evolution of the pH, which enabled the tracking of TA and dissolved inorganic carbon DIC in real time. Figure 3 shows a single electrochemical carbon capture cycle using 0.5 M 1,8-ESP in the negolyte. In this cycle, pure CO<sub>2</sub> was separated from a mixture of 10% CO<sub>2</sub> and 90% N<sub>2</sub> through a deacidification + CO<sub>2</sub> absorption process, followed by acidification + CO<sub>2</sub> outgassing process. When applying a positive 20 mA cm<sup>-2</sup> current at *t* (time) = 2 h (Fig. 3a), charging the cell, the electrochemically induced deacidification process began and so did CO<sub>2</sub> absorption, evidenced by the decreased downstream CO<sub>2</sub> partial pressure (*p*CO<sub>2</sub>) (Fig. 3f) and gas flow rate (Fig. 3g). The deacidification process lasted from *t* = 2 h until *t* = 4.5 h when the voltage reached the programmed cut-off value of 1.4 V (Fig. 3b). During deacidification, TA increased linearly as an effect of galvanostatic charging, whereas the pH, although still increasing because of increasing hydroxide concentration, was buffered by the absorbed CO<sub>2</sub> and the subsequently formed carbonate and bicarbonate. Had there not been any CO<sub>2</sub> presence in the feed gas stream, the pH would have reached 14 at the end of deacidification. CO<sub>2</sub> absorption continued to occur until *t* = 12 h, as indicated by the fact that both downstream flow rate (Fig. 3g) and *p*CO<sub>2</sub> (Fig. 3f) took that long to return to baseline. The flat regions in voltage (Fig. 3b) and pH (Fig. 3d) in between *t* = 12 and 13 h also suggest the absorption reaction was in a steady-state regime.

The acidification + CO<sub>2</sub> outgassing process started at *t* = 15 h, when a negative 20 mA cm<sup>-2</sup> current was applied (Fig. 3a). Unlike the deacidification + CO<sub>2</sub> absorption process, where the electrochemical reaction outpaced the chemical reaction significantly, the acidification and CO<sub>2</sub> outgassing had almost the same duration (*t* = 15 to 17.3 h). This difference suggests that the deacidification + CO<sub>2</sub> absorption process is rate limited by CO<sub>2</sub> absorption and the acidification + CO<sub>2</sub> outgassing process is rate limited by the acidification rate, which is controlled by the current density. In this particular half cycle, the CO<sub>2</sub> outgassing rate was 2.2 ml min<sup>-1</sup> (14–11.8 ml min<sup>-1</sup> baseline).

The effective amount of separated CO<sub>2</sub> could be calculated by integrating the difference between flow rate and the baseline (Fig. 3g) over the CO<sub>2</sub> capture or outgassing region and then subtracting the net amount captured and released in the transients during gas changes (for example, *t* = 13 to 13.3 h and *t* = 26 to 26.3 h) (ref. 23). In this cycle, 8.4 mmol or—assuming, throughout this paper, standard conditions of *T* (temperature) = 293 K, *p* (pressure) = 1 bar and ideal gas behaviour—202 ml of CO<sub>2</sub> was separated from a 10% inlet and concentrated to a 100% exit (Fig. 3e). The work input during deacidification was 917 J, calculated from integrating the product of current (Fig. 3a) and voltage (Fig. 3b) in between *t* = 2 h and *t* = 4.5 h. Similarly, the work returned during acidification was 479 J. Therefore, the overall cycle work was

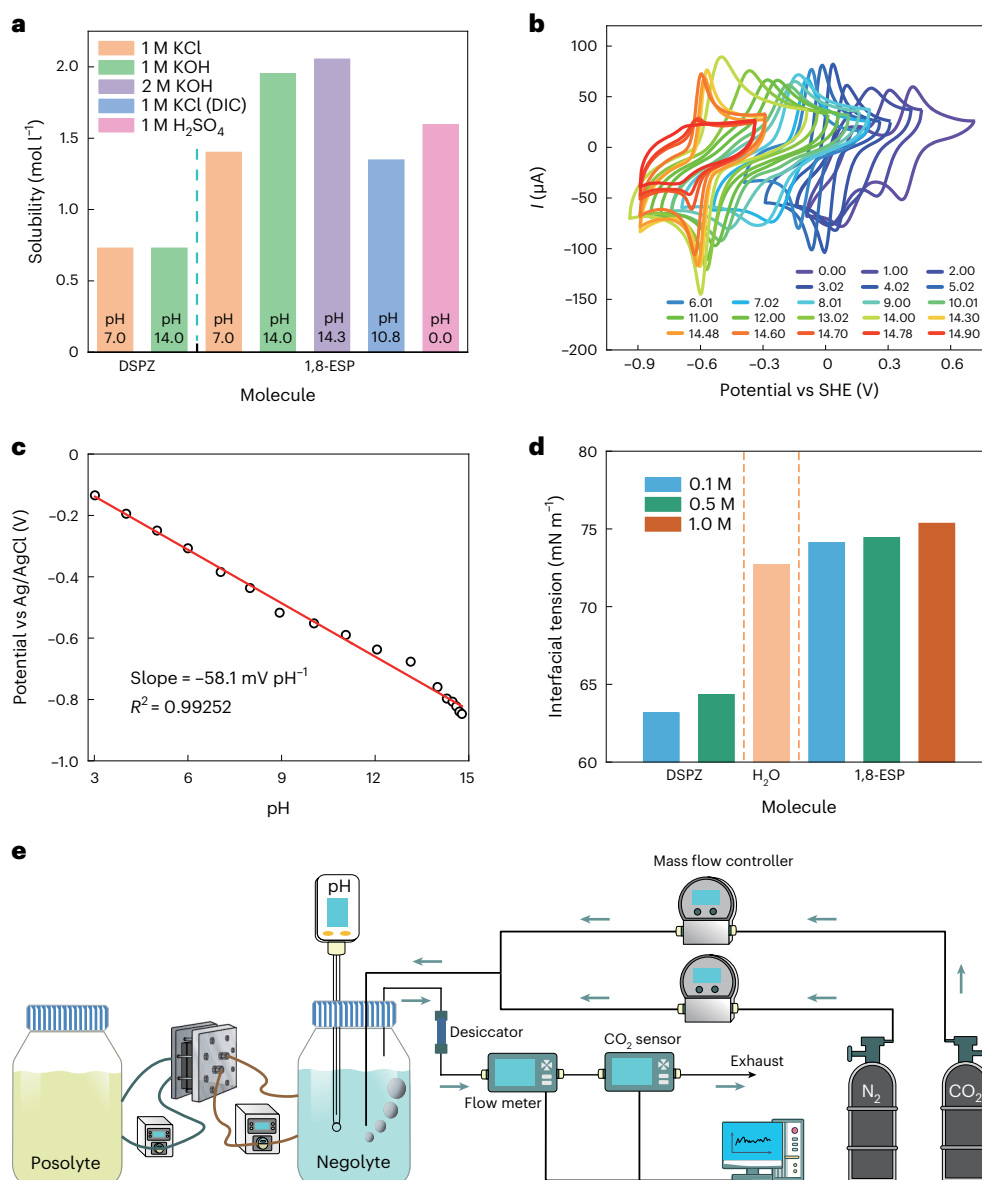


**Fig. 2 | Molecular property study and schematic of the CO<sub>2</sub> capture/release system.** **a**, Solubility of 1,8-ESP and DSPZ in different electrolytes. **b**, CV curves of 1,8-ESP in different pH buffer solutions with 1.0 M KCl. *I* is the current intensity, SHE represents the standard hydrogen electrode. **c**, Pourbaix diagram of 1,8-ESP.

The data points are fitted with a line using a linear fit, where  $y = -0.0581x + 0.2466$ ,  $R^2 = 0.99252$ . **d**, Interfacial tension of 1,8-ESP, H<sub>2</sub>O and DSPZ with different concentrations at 20 °C. **e**, Scheme of Fe(CN)<sub>6</sub> (posolyte) | 1,8-ESP (negolyte) flow cell for CO<sub>2</sub> capture/release experiments. The blue arrows indicate gas flow.

438 J and the CO<sub>2</sub> molar cycle work was 52 kJ mol<sub>CO<sub>2</sub></sub><sup>-1</sup>, which is obtained by dividing the cycle work by the effective amount of separated CO<sub>2</sub>. This value is modest compared with commercial amine-scrubbing processes<sup>35</sup> and is lower than that of the DSPZ cell, 61 kJ mol<sub>CO<sub>2</sub></sub><sup>-1</sup>, at the same current density<sup>23</sup>. In addition to the molar energetic cost, the rate of capture and outgassing also affects the cost of the process at scale. In this cycle, the maximum CO<sub>2</sub> flow into the solution during capture was 0.7 ml<sub>CO<sub>2</sub></sub> min<sup>-1</sup> or 0.07 ml<sub>CO<sub>2</sub></sub> min<sup>-1</sup> per ml of solution and the max CO<sub>2</sub> outflow during outgassing was 1.8 ml<sub>CO<sub>2</sub></sub> min<sup>-1</sup> or 0.18 ml<sub>CO<sub>2</sub></sub> min<sup>-1</sup> per ml of solution. Conditions that influence the rate and optimization methods are discussed later in the text.

The effect of current density and negolyte concentration on energy, capacity and capture/outgassing rate were explored next. Supplementary Fig. 26 shows 30 electrochemical carbon-separation cycles done under varying current densities and 1,8-ESP concentrations. As the concentration of 1,8-ESP increases, it takes longer to finish each cycle because of increased electron capacity and higher TA. Consequently,

**Table 1 | Summary of the electrochemical and physico-chemical properties of 1,8-ESP**

1,8-ESP <sup>a</sup>	<i>E</i> <sub>1/2</sub> vs SHE (V) <sup>b</sup>	Solubility (mol l <sup>-1</sup> )	<i>D</i> (cm <sup>2</sup> s <sup>-1</sup> ) <sup>c</sup>	<i>k</i> <sub>0</sub> (cm s <sup>-1</sup> ) <sup>d</sup>
1.0 M KOH	-0.503	1.95	2.78 × 10 <sup>-5</sup>	1.15 × 10 <sup>-3</sup>
2.0 M KOH	-0.590	2.06	2.52 × 10 <sup>-5</sup>	1.97 × 10 <sup>-3</sup>
1.0 M KCl	-0.390	1.40	3.25 × 10 <sup>-5</sup>	8.65 × 10 <sup>-4</sup>
1.0 M KCl <sup>e</sup>	-0.370	1.35	2.46 × 10 <sup>-5</sup>	1.24 × 10 <sup>-4</sup>
1.0 M H <sub>2</sub> SO <sub>4</sub> <sup>f</sup>	0.393 <sup>g</sup>	1.60	1.10 × 10 <sup>-5g</sup>	4.25 × 10 <sup>-5g</sup>
	0.118 <sup>h</sup>		3.10 × 10 <sup>-5h</sup>	4.92 × 10 <sup>-5h</sup>

<sup>a</sup>Measured at room temperature. <sup>b</sup>Redox potential. *E*<sub>1/2</sub> is the half-wave potential, SHE represents the standard hydrogen electrode. <sup>c</sup>Diffusion coefficient. <sup>d</sup>Electron transfer rate constant. <sup>e</sup>With 0.436 M K<sub>2</sub>CO<sub>3</sub> and 0.128 M KHCO<sub>3</sub> (1.0 M KOH saturated with 0.4 mbar CO<sub>2</sub>). <sup>f</sup>The reduction of 1,8-ESP in 1.0 M H<sub>2</sub>SO<sub>4</sub> exhibits a two-step process (Fig. 2b and Supplementary Fig. 13). <sup>g</sup>The value for the first step. <sup>h</sup>The value for the second step.

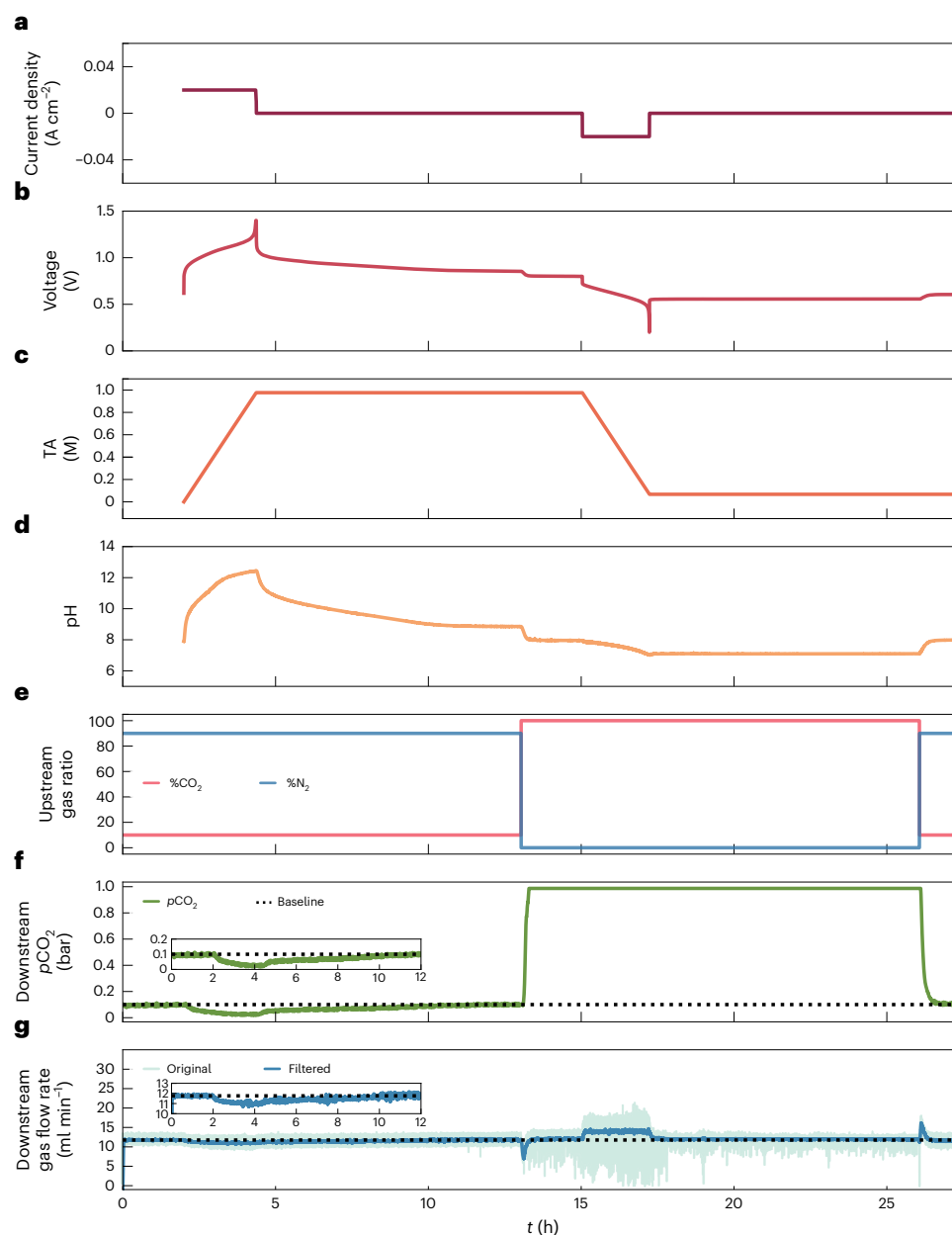


**Fig. 3 | A CO<sub>2</sub> concentrating cycle using a 1,8-ESP-based flow cell.** The inlet partial pressure was  $p_1 = 0.1$  bar and the exit pressure was  $p_3 = 1$  bar. The cell was assembled with a Fumasep E-620 (K) membrane and carbon papers (Sigracet SGL 39AA) electrode. Electrolytes comprised 10 ml 0.5 M 1,8-ESP in 1.0 M KCl (negolyte, capacity limiting) and 35 ml 0.3 M K<sub>4</sub>Fe(CN)<sub>6</sub> and 0.1 M K<sub>3</sub>Fe(CN)<sub>6</sub> in 1.0 M KCl (posolyte, non-capacity limiting). The cell was cycled galvanostatically at 20 mA cm<sup>-2</sup> with a voltage cut-off between 1.4 V and 0.2 V and each half cycle ended with a potentiostatic hold until the magnitude of the current density fell below 1 mA cm<sup>-2</sup>. The feed gas was 10% CO<sub>2</sub> for the capture step and switched

to pure CO<sub>2</sub> for the sweep step. **a**, Current density. **b**, Voltage. **c**, Total alkalinity. **d**, pH of the negolyte. **e**, N<sub>2</sub> and CO<sub>2</sub> percentage in the upstream source gas, controlled by mass flow controllers. **f**, Downstream CO<sub>2</sub> partial pressure. The baseline indicates  $p_{\text{CO}_2} = 0.1$  bar. Inset: zoomed-in view of downstream CO<sub>2</sub> partial pressure in between 0 <  $t$  < 12 h, where CO<sub>2</sub> capture takes place. **g**, Downstream total gas flow rate; the baseline is 11.8 ml min<sup>-1</sup>. Inset: zoomed-in view of downstream gas flow rate (filtered with a Savitzky–Golay filter<sup>56</sup>. The integrals of the filtered and the unfiltered data are the same) in between 0 <  $t$  < 12 h, where CO<sub>2</sub> capture takes place.

more CO<sub>2</sub> can be captured per unit volume, as shown in Fig. 4a. With a 0.8 M 1,8-ESP solution, a CO<sub>2</sub> capacity of close to 1.4 mol<sub>CO<sub>2</sub></sub> l<sup>-1</sup> or 1.8 mol<sub>CO<sub>2</sub></sub> per mol<sub>1,8-ESP</sub> is achieved. Such CO<sub>2</sub> loading per active material is comparable to the loading in the amine-scrubbing process, although the concentration of amines can be higher<sup>35,36</sup>. Changing current densities does not change the capacity, but it has a substantial impact on the CO<sub>2</sub> ingassing rate during deacidification + capture and outgassing rate during acidification + desorption. The magnitude of both absorption flow and outgassing flow decreases as current density decreases (Fig. 4b) because current density determines the rate of TA formation

or consumption. The magnitude of peak absorption flow increases with 1,8-ESP concentration because the rate of CO<sub>2</sub> absorption is augmented by the increased hydroxide concentration<sup>37</sup>, which results from a higher 1,8-ESP concentration. This trend is more obvious at higher current densities, as more hydroxides can be accumulated due to the sluggish hydroxide-CO<sub>2</sub> reaction. In contrast, the max outgassing flow does not change significantly across the three concentrations because, unlike the absorption case, the rate of hydroxide consumption, that is, current density, is the rate-limiting reaction in the acidification + desorption process. To increase overall productivity, that is, CO<sub>2</sub> separation



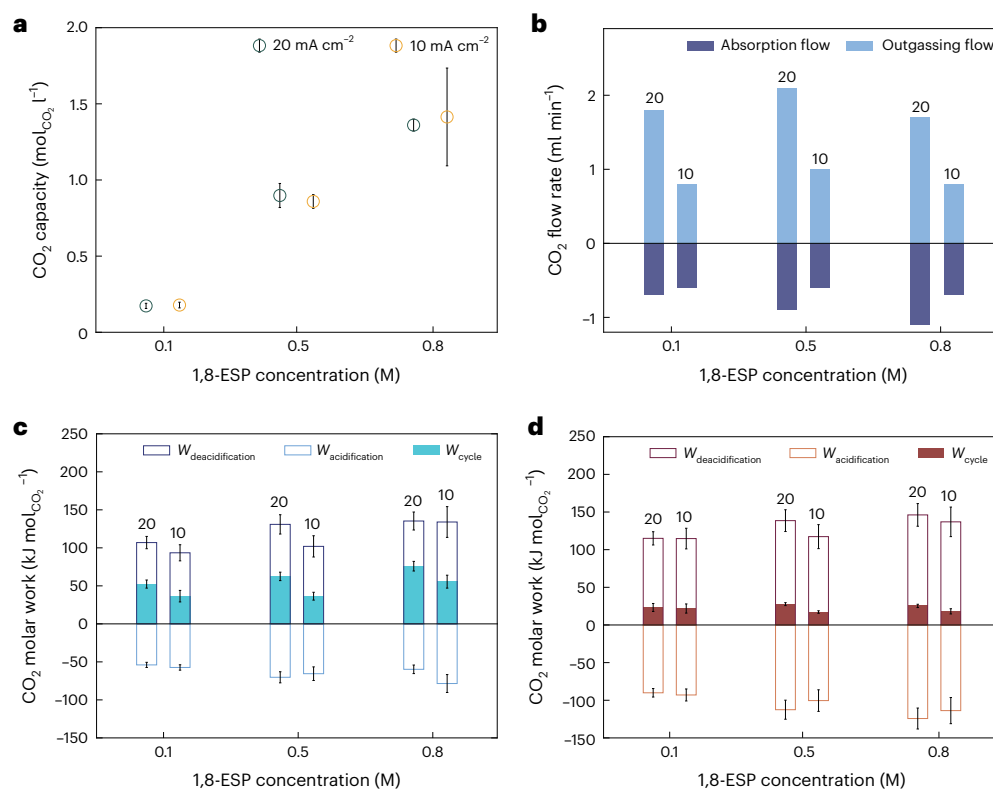


**Fig. 4 | CO<sub>2</sub> separation performance at different 1,8-ESP concentrations and current densities.** The error bars represent standard deviation calculated over five cycles under each condition ( $n = 5$ ). The central measure used for the error bars is the median with standard deviation. **a**, CO<sub>2</sub> capacity per litre solution. **b**, Max CO<sub>2</sub> outgassing rate during acidification + desorption (positive) and max

CO<sub>2</sub> ingassing rate during deacidification + absorption (negative). **c**, CO<sub>2</sub> molar deacidification, acidification and cycle work obtained under alternating 10% CO<sub>2</sub>/90% N<sub>2</sub> during deacidification and 100% CO<sub>2</sub> during acidification. **d**, CO<sub>2</sub> molar deacidification, acidification and cycle work when the cell was cycled in a pure N<sub>2</sub> atmosphere.

**Table 2 | Summary of cell metrics at different 1,8-ESP concentrations and current densities illustrated in Supplementary Fig. 19**

Concentration (M)	Current density (mA cm <sup>-2</sup> )	Cycle work (kJ mol <sub>CO<sub>2</sub></sub> <sup>-1</sup> )	Max absorption/desorption flow rate (ml min <sup>-1</sup> )	CO <sub>2</sub> capture capacity (mol <sub>CO<sub>2</sub></sub> l <sup>-1</sup> )	Discharge capacity (Ah l <sup>-1</sup> ) <sup>a</sup>	Capacity fade rate (% per day)
0.1	20	52	-0.7/1.8	0.18	5.0	0.00 <sup>b</sup> (0.00) <sup>c</sup>
	10	36	-0.6/0.8	0.17		
0.5	20	63	-0.9/2.1	0.90	22.2	0.01 <sup>d</sup>
	10	36	-0.6/1.0	0.86		
0.8	20	76	-1.1/1.7	1.36	42.7	0.01 <sup>e</sup>
	10	55	-0.7/0.8	1.41		

The feed gas was a mixture of 0.1 bar CO<sub>2</sub> and 0.9 bar N<sub>2</sub> for the capture step and switched to pure CO<sub>2</sub> for the sweep step. <sup>a</sup>Negolyte volumetric capacity, galvanostatic–potentiostatic cycling.

<sup>b</sup>Under nitrogen atmosphere, illustrated in Fig. 5a. <sup>c</sup>Under pure CO<sub>2</sub> atmosphere, illustrated in Fig. 5b. <sup>d</sup>Under nitrogen atmosphere, illustrated in Supplementary Fig. 25a. <sup>e</sup>Under nitrogen atmosphere, illustrated in Supplementary Fig. 25b.

per unit time, it is essential to raise the CO<sub>2</sub> capture rate because it is significantly slower than the outgassing rate. One method is to use a contactor engineered for high gas–solution interaction surface area<sup>13</sup>. An alternative strategy is to incorporate promoters, molecules that enhance the CO<sub>2</sub> capture rate of caustic solutions<sup>38</sup>. Another approach involves heating the solution, but this may compromise capacity<sup>39</sup>.

The CO<sub>2</sub> molar work cost of the carbon capture cycles (Fig. 4c) is compared with that of the cycles performed under N<sub>2</sub> (Fig. 4d). The latter represents the energy loss caused by internal cell dissipation, that is, only ohmic, electron transfer and mass transport losses; it is evaluated by dividing the measured deacidification, acidification and cycle work in the absence of CO<sub>2</sub> by the amount of captured CO<sub>2</sub> measured in the carbon capture cycle of the same current density and 1,8-ESP concentration. The deacidification work of the cycles under

CO<sub>2</sub> is lower than that of the CO<sub>2</sub>-free cycles because CO<sub>2</sub> absorption decreases the negolyte pH, thereby decreasing the overall cell voltage. The same mechanism decreases the magnitude of the returned work during acidification in the cycles under CO<sub>2</sub>. The average pH during deacidification is around 10.5 and 13.5 for CO<sub>2</sub> and N<sub>2</sub> cycling, respectively, whereas the average pH during acidification is around 7.5 and 13.5, respectively. The greater pH gap during acidification, caused by higher CO<sub>2</sub> partial pressure in the head space, causes a net increased cycle work. As the concentration of 1,8-ESP increases, the pH gap in acidification increases, which leads to a positive correlation between 1,8-ESP concentration and cycle work.

Lower current density also leads to lower cycle work because of smaller cell dissipation losses. It is noteworthy that 36 kJ mol<sub>CO<sub>2</sub></sub><sup>-1</sup> CO<sub>2</sub>, a remarkably low value, is achieved at both 0.1 and 0.5 M using 10 mA cm<sup>-2</sup>

current density. Table 2 summarizes the capture cell properties studied in this work. At low 1,8-ESP concentration, only a minimal amount of capture work is needed to drive the cycle, but this comes at the cost of volumetric capture capacity and reaction rate. At high concentration, capture capacity can be an order of magnitude higher, and the rate is faster, but the molar cycle work increases: increased cell resistance is expected when the solution viscosity increases (Supplementary Table 4). We also studied the time dependence of CO<sub>2</sub> absorption and energetic cost at various concentrations and current densities (Supplementary Figs. 27–29) and observed that the capture turnover rate might be increased by 20% without significantly raising the cost.

## Stability investigation of carbon capture cells

Although various CO<sub>2</sub> capture methods with promising performance have been achieved, few studies have addressed the operational lifetime of such device, and the stability of CO<sub>2</sub> capture material remains a major challenge. We investigated the chemical stability of 1,8-ESP carefully through elevated temperature chemical degradation studies. 1,8-ESP solution at 45 °C was monitored by time-dependent NMR spectroscopy, and no chemical decomposition is found over more than 100 days from the NMR spectra (Supplementary Fig. 30a). We attribute such high molecular stability to the chemically inert carbon linkage between the soluble functional groups ( $-SO_3H$ ) and the phenazine core in the structure of 1,8-ESP. It avoids the decomposition from nucleophilic substitution and hydrolysis of the molecule<sup>31,40</sup>. It has been observed in our previous work that the reduced state of phenazine derivatives tends to tautomerize and lose its reversible redox activities<sup>41,42</sup>. The *re*-1,8-ESP (reduced state of 1,8-ESP) at 45 °C was compared with an internal standard, showing no degradation (Supplementary Fig. 30b). DFT theoretical study corroborated the chemical stability of 1,8-ESP in its reduced state whose standard free energy of tautomerization ( $\Delta G$ ) is calculated to be  $>45 \text{ kJ mol}^{-1}$  (Supplementary Note 2 and Supplementary Table 2), excluding the tautomerization pathway.

We investigated long-term cycling stability of a 1,8-ESP cell in 0.1 M by imposing 550 charge–discharge cycles over 16 days under nitrogen atmosphere. Cycles began with a galvanostatic process at  $20 \text{ mA cm}^{-2}$  until voltage limits of 1.4 V on charging and 0.4 V on discharging were reached, followed by potentiostatic processes that lasted until the magnitude of the current density fell to  $4 \text{ mA cm}^{-2}$ . The cell exhibited no perceptible capacity fade, which is in agreement with the absence of chemical decomposition products detected after cycling by NMR (Fig. 5a and Supplementary Fig. 31). Both 0.5 M and 0.8 M 1,8-ESP cells showed an extremely low fade rate<sup>27</sup> of around 0.01% per day during 14 days of testing (Supplementary Fig. 32 and Table 2), but if this fade rate were to continue unchanged, it would be low enough for decadal implementation. The compatibility of 1,8-ESP with CO<sub>2</sub> is also vital to the system lifetime as it has been reported that a significant number of molecules can bind with CO<sub>2</sub> and precipitate out from the solution<sup>43</sup> or enhance molecular decomposition<sup>44</sup>. The operational stability of the 1,8-ESP carbon capture system was investigated with capture–release cycles with pure CO<sub>2</sub> (99.9%) as the feed gas (Fig. 5b). During 220 cycles over 18 days, the voltage profiles reflecting the continuous CO<sub>2</sub> capture and release processes exhibited high reproducibility. No precipitation occurred and no chemical decomposition products were detected by NMR, indicating compatibility of 1,8-ESP with CO<sub>2</sub> (Supplementary Figs. 33–35). The system stability is also exhibited in the retention of the discharge capacity: no discharge capacity decay was observed during cycling, suggesting excellent system stability.

The stability of carbon capture cells against O<sub>2</sub> is also critical to their practical deployment for either flue gas capture or direct air capture, which contains 3–5% and 20% O<sub>2</sub>, respectively. We tested 1,8-ESP carbon capture cells with capture–release cycles with CO<sub>2</sub> (20%) and 3–20% O<sub>2</sub> as the feed gas. Excess posolyte permits us to focus our attention on the chemical stability of only the negolyte. Under 3% O<sub>2</sub> concentration, the cell showed no apparent<sup>27</sup> capacity

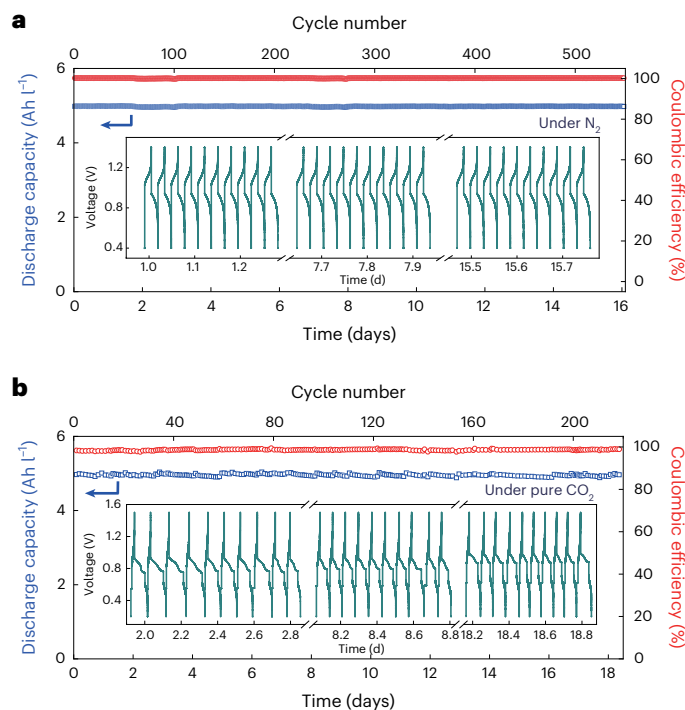


**Fig. 5 | Cycling performance of 0.1 M 1,8-ESP full cell.** Negolyte: 7 ml 0.1 M 1,8-ESP in 1.0 M KCl. Posolyte: 40 ml 0.1 M  $K_4Fe(CN)_6$  and 0.02 M  $K_3Fe(CN)_6$  in 1.0 M KCl solution. The cell was assembled with a Nafion NC700 membrane and carbon clothes (ELAT-Hydrophilic) electrode. **a, b**, The cell was cycled galvanostatically at  $20 \text{ mA cm}^{-2}$  with a voltage cut-off, and each half cycle ended with a potentiostatic hold until the magnitude of the current density fell below  $4 \text{ mA cm}^{-2}$ , voltage cut-off of 1.4 V and 0.4 V under N<sub>2</sub> (**a**) and voltage cut-off of 1.5 V and 0.2 V with CO<sub>2</sub> capture and release cycles with pure CO<sub>2</sub> as the feed gas during the whole process (**b**). The red and blue symbols represent Coulombic efficiency and discharged capacity, respectively, and the insets show representative voltage versus time curves. The x-axis breaks in the insets indicate discontinuities in the axis lines, which are implemented to enhance the visual manageability of the charge–discharge curves.

decay (Supplementary Fig. 36) with an average Coulombic efficiency of 95% (Fig. 6a and Supplementary Table 5). This high Coulombic efficiency indicated the robustness of 1,8-ESP against O<sub>2</sub> impurity, which is comparable to the reported carbon capture molecules<sup>45</sup>. When the O<sub>2</sub> concentration increased to 10% and 20%, no apparent discharge capacity decay was observed, and the average Coulombic efficiency remained reasonably high at 89% and 82%, respectively. It is a major advance compared to DSPZ cell with an ~65% Coulombic efficiency under 20% O<sub>2</sub> (Supplementary Fig. 37)<sup>23</sup>.

The chemical oxidation of *re*-1,8-ESP by O<sub>2</sub> is reversible and so can be counteracted by an electrochemical reduction; however, the additional pulse of electrochemical reduction simultaneously oxidizes the posolyte, and the cell will go out of balance, accumulating oxidized species in the posolyte and DIC in the negolyte. Effective cell rebalancing can be accomplished and the original chemical compositions of both electrolytes restored by reverse polarization<sup>23</sup>, driving the oxygen evolution reaction in the negolyte reservoir. There is an additional energy cost when the electrochemical rebalancing is applied, but if the negolyte molecule is less air sensitive and the cell exhibits high Coulombic efficiency, the energy cost is minimized. Under 3% O<sub>2</sub>, the energy cost of the 1,8-ESP cell with the electrochemical rebalancing is calculated to be  $38 \text{ kJ mol}_{CO_2}^{-1}$ , assuming that the ratio of rebalancing cost to cycle work is the same as reported in previous work<sup>23</sup>. Because of the high Coulombic efficiency, the cost penalty is only  $3 \text{ kJ mol}_{CO_2}^{-1}$ , which is less than 10% of the cycle work of  $35 \text{ kJ mol}_{CO_2}^{-1}$  without

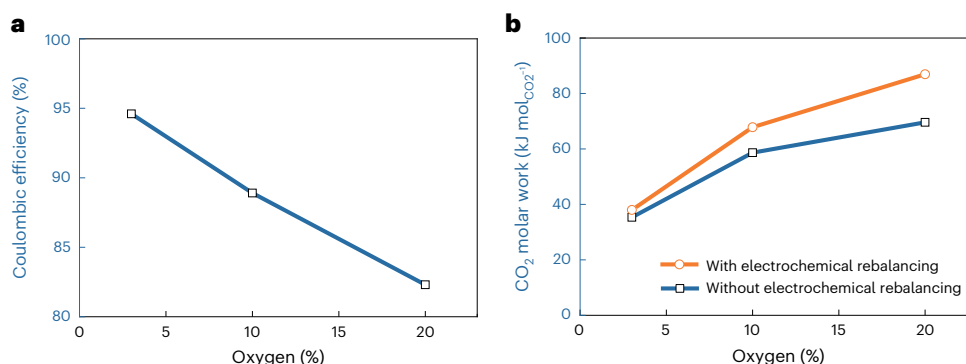


**Fig. 6 | CO<sub>2</sub> capture cells under different oxygen concentrations.** **a**, Coulombic efficiency. **b**, CO<sub>2</sub> molar work. The full cell test was conducted with the galvanostatic cycle at 20 mA cm<sup>-2</sup> with a voltage cut-off between 1.5 V and 0.2 V. Besides different oxygen content shown in Supplementary Fig. 36, the feed gas

contained 20% CO<sub>2</sub> complemented with N<sub>2</sub> and a 2 sccm flow rate was applied during both deacidification + CO<sub>2</sub> absorption and acidification + CO<sub>2</sub> release processes.

electrochemical rebalancing (Fig. 6b and Supplementary Table 5). Under 20% O<sub>2</sub>, the cost without and with rebalancing increases to 70 kJ mol<sub>CO<sub>2</sub></sub><sup>-1</sup> and 87 kJ mol<sub>CO<sub>2</sub></sub><sup>-1</sup>, as the lower Coulombic efficiency led to less CO<sub>2</sub> capture and a higher rebalancing cost. Nevertheless, it is still at the low end of energy cost among all systems.

## Energy storage performance when isolated from CO<sub>2</sub> capture

Finally, we investigated the performance of the cell as a pure energy storage system when isolated from CO<sub>2</sub>. The asymmetric charge–discharge cycling and reverse polarity at intermediate SOC<sub>s</sub> were performed, indicating good cycling reversibility of the cell (Supplementary Fig. 38). In Supplementary Fig. 39, we show the polarization and long-term cycling performance of a 1,8-ESP cell with 2.0 M electron concentration, corresponding to a negolyte volumetric capacity of 54.0 Ah l<sup>-1</sup>. The theoretical volumetric capacity of the battery overall was 10.7 Ah l<sup>-1</sup>, limited by the solubility of potassium ferrocyanide (0.5 M at pH 14) (ref. 31) on the positive side. The cell exhibited an average open-circuit voltage exceeding 1.1 V. When a current density at 20 mA cm<sup>-2</sup> was applied in purely galvanostatic cycling, the Coulombic efficiency was above 99.9% and the capacity utilization reached 92.6% with a round-trip energy efficiency of 78.5%. We first applied galvanostatic cycling for approximately ten days with no obvious capacity fade observed. This was then followed by a galvanostatic–potentiostatic cycling regimen, which accesses almost all of the theoretical capacity (95%) for ~170 days, with a low capacity fade rate of 0.008% per cycle (0.05% per day), demonstrating its excellent performance to be among those of state-of-the-art flow batteries<sup>27</sup>. The operator would have the flexibility of timing cell charging and discharging based on electricity prices with the added flexibility of either exposing the electrolyte to CO<sub>2</sub> for capture or isolating the electrolyte from CO<sub>2</sub> to maximize instantaneous revenue from energy storage.

## Conclusions

In this work, an electrochemical CO<sub>2</sub> capture system with coupled electricity storage based on a 1,8-ESP flow cell is developed and is demonstrated to possess high capacity, high stability and low energetic cost. The CO<sub>2</sub> capture system with 0.8 M 1,8-ESP exhibits a volumetric CO<sub>2</sub> capture capacity of 1.4 mol<sub>CO<sub>2</sub></sub> l<sup>-1</sup> with an energetic cost of 55 kJ mol<sub>CO<sub>2</sub></sub><sup>-1</sup> at 10 mA cm<sup>-2</sup>. CO<sub>2</sub> capture–release cycling under 3–20% O<sub>2</sub> with 95–82% Coulombic efficiency indicates the good stability of the carbon capture system for O<sub>2</sub>-rich feed gas. The cell offers high performance as a pure energy storage device when isolated from CO<sub>2</sub>, which enables the operator to increase revenue by operating purely for electricity price arbitrage when market conditions call for it and implementing

CO<sub>2</sub> capture at other times. A 220-cycle cell test with continuous CO<sub>2</sub> capture and release over 18 days left no evidence of chemical decomposition in the electrolyte; a 1,200-cycle cell test for pure energy storage performance with a negolyte capacity of 54.0 Ah l<sup>-1</sup> over 180 days exhibited a low capacity fade rate of 0.05% per day. These results show that 1,8-ESP can be the basis of a high-performance system for CO<sub>2</sub> capture, energy storage or both.

## Methods

### Materials

Unless otherwise stated, all chemicals were obtained from commercial sources and utilized without additional purification. Air-sensitive reactions were carried out in oven-dried glassware by using standard Schlenk techniques.

### Synthesis of 1,8-ESP

**Step 1:** to a 350 ml high-pressure flask, 1,8-dibromo-phenazine (20 mmol, 1.0 equivalent), Vinylsulfonic acid sodium aqueous solution (25 wt% in water, approximately 2.3 mol l<sup>-1</sup>, 2.5 equivalent), PdCl<sub>2</sub> (2 mol %), Tri(*o*-tolyl)-phosphine (4 mol %), Et<sub>3</sub>N (2.5 equivalent) and dimethyl formamide (DMF) (80 ml) were added, then the flask was sealed under N<sub>2</sub> atmosphere and the mixture was heated and stirred at 100 °C for 12 h. The mixture was gradually cooled to room temperature, then absolute ethyl alcohol (15 ml) was added and further stirred evenly. Dichloromethane (DCM) (100 ml) was then added to the mixture and a large amount of yellow-green solids were precipitated. The precipitations were collected by filtration, washed with DCM to remove the residual DMF and further dried under vacuum to obtain a yellow-green solid and were used for the next step without further purification.

**Step 2:** to a 100 ml polyvinylidene fluoride (PVDF) flask that matched with the high-pressure hydrogenation reactor, above-mentioned crude products, Pd/C (5% on carbon), H<sub>2</sub>O (15 ml), MeOH (30 ml) were added in air. The high-pressure hydrogenation reactor was sealed and filled with 30 bar hydrogen, then the mixture was stirred vigorously for 2.5 h at room temperature. Pd/C was removed by a 2.5 μm filter to obtain a clear solution. The filtrate was concentrated and purified via reversed phase column chromatography using 2–5% MeOH in H<sub>2</sub>O to collect product 1,8-ESP as a yellow solid (89% yield). Data for <sup>1</sup>H NMR were recorded as follows: chemical shifts δ were reported in ppm, coupling constant(s) *J* in Hz and multiplicities are recorded as s = singlet, dd = doublet of doublets, m = multiplet or unresolved. <sup>1</sup>H NMR (600 MHz, D<sub>2</sub>O) δ 7.41 (dd, *J* = 8.6, 6.7 Hz, 1H), 7.38–7.30 (m, 4H), 7.27 (dd, *J* = 6.7, 1.3 Hz, 1H), 3.28–3.23 (m, 2H), 3.19 (s, 4H), 3.11–3.06 (m, 2H). The detailed characterization data is in Supplementary Note 1.



## Solubility tests

The solubility of ESP molecules was measured by adding the ESP compounds into the corresponding electrolyte solutions until no further solids could be dissolved. The saturated solution of ESPs was obtained by removing the supernatant after centrifugation. The saturated solution was then diluted by a known amount of it, and its concentration was determined by UV-vis spectrophotometry (Agilent Cary 60 spectrometer). The concentration was calculated according to a pre-calibrated absorbance versus concentration curve of known ESP concentrations.

## Permeability measurements

The permeability of the 1,8-ESP across a NC700 membrane and Nafion212 was evaluated using a commercially customer-made electrolyser with two-compartment cell. The donating side of the cell was filled with 0.1 M 1,8-ESP in KCl (1.0 M), while the receiving side was filled with the same volume of 1.0 M KCl. Both sides of the cell were continuously stirred during the measurements. The solution was taken out from the receiving side at different time intervals for UV-vis spectrophotometry and subsequently returned to the receiving side after characterizing. The concentration was calculated from a calibration curve of UV-vis absorption at different concentration and the permeability of 1,8-ESP was calculated based on Fick's law as the equation<sup>31,46,47</sup>:

$$P = \frac{\Delta \ln(1 - \frac{C_t}{C_0}) (\frac{V_0}{2A})}{\Delta t}$$
, where  $P$  is permeability ( $\text{cm}^2 \text{s}^{-1}$ ),  $A$  is the effective membrane area ( $\text{cm}^2$ ),  $t$  is elapsed time (s),  $C_t$  ( $\text{mol l}^{-1}$ ) is the concentration of 1,8-ESP, which has crossed the membrane from the donating side and is detected by the UV-Vis at time  $t$ ,  $V_0$  is the volume of the solution in either compartment ( $5 \text{ cm}^3$ ),  $l$  is the thickness of the NC700 membrane ( $15 \mu\text{m}$ ) or Nafion 212 ( $51 \mu\text{m}$ ),  $C_0$  is the concentration of 1,8-ESP in the donating side at time zero ( $0.1 \text{ mol l}^{-1}$ ) and  $\Delta$  represents a finite difference.

## Electrochemical characterization

An Ag/AgCl reference electrode filled with 3.0 M KCl salt bridge solution, a platinum wire auxiliary counter electrode and a 5 mm glassy carbon working electrode were used for all three-electrode cyclic voltammograms (CV) tests. CV and rotating disk electrode (RDE) measurements were both conducted with 5 mM ESP in different supporting electrolytes at a sweep rate of  $20 \text{ mV s}^{-1}$ . The RDE curves were obtained with a Pine Instruments Modulated Speed Rotator AFM-SRCE equipped with a 5 mm diameter rotation disk electrode and recorded on a BioLogic VSP-300 instrument. An Ag/AgCl electrode (filled with 3.0 M KCl) was used as the reference electrode, and a platinum wire was used as the counter electrode. The diffusion coefficient ( $D$ ) was determined by the slope of fitted Levich equation<sup>48</sup>:  $i_{\text{lim}} = 0.620 n F A C D^{2/3} \nu^{-1/6} \omega^{1/2}$ , where  $n = 2$ , Faraday's constant  $F = 96,485 \text{ C mol}^{-1}$ ,  $A$  (electrode area) =  $0.196 \text{ cm}^2$ , ESP concentration  $c = 5 \times 10^{-6} \text{ mol cm}^{-3}$  and kinetic viscosity  $\nu = 0.01 \text{ cm}^2 \text{s}^{-1}$ .

The rate constant ( $k_0$ ) of ESP was calculated from the Tafel equation<sup>49</sup>:  $\log_{10}(i) = \log_{10}(n F A k_0) + \frac{anF\eta}{2.303RT}$ , where  $n$  is the number of electrons in the rate-limiting step ( $n = 1$ ),  $R$  (universal gas constant) =  $8.314 \text{ J K}^{-1} \text{mol}^{-1}$ ,  $T$  (temperature) =  $293.15 \text{ K}$ .

## Flow cell setup

All flow cells were assembled with graphite runner for electrolyte flowing, cation-exchange membrane as separator, Sigracet SGL 39AA carbon paper (thickness  $280 \mu\text{m}$ ) or ELAT-Hydrophilic carbon cloth (thickness  $406 \mu\text{m}$ ) as electrode (geometric surface area  $5 \text{ cm}^2$ ), Viton (PVDF) gaskets for sealing the flow cell and two copper current collectors. Flow of electrolytes was driven by a peristaltic pump. A Mettler Toledo pH electrode (LE422) was implemented for monitoring the electrolyte pH. The flow meter utilized in the downstream region of the negolyte headspace was a Servoflo FS4001-100-V-A, and the  $\text{CO}_2$  sensor employed was an ExplorIR-W 100%  $\text{CO}_2$  sensor, acquired from co2meter.com. All electrochemical characterization was conducted and recorded on a BioLogic VSP-300 or BCS-128 instrument.

## $\text{CO}_2$ capacity utilization and extra energy cost

The trade-off between  $\text{CO}_2$  capacity utilization during the capture process and the capture kinetics for each cycling condition are shown in Supplementary Figs. 20–22. The horizontal axis refers to the percentage of time elapsed relative to the duration of the entire capture period set in the protocol. The vertical axes represent the capacity utilization and extra energy needed, as percentages relative to the values achieved at the end of the capture period. The first point in each diagram indicates the completion point of an electrochemical deacidification. There is a roughly logarithmic trend in each of the capacity-loading-vs-time diagrams, indicating a decrease in kinetics as the pH drops. The  $\text{CO}_2$  molar cycle work, measured in  $\text{kJ mol}_{\text{CO}_2}^{-1}$ , is higher when the sorbent capacity is not fully utilized. This is because the cycle work, measured in kJ, stops changing once the electrochemical deacidification is complete, whereas the amount of captured  $\text{CO}_2$ , measured in mol, is smaller when the allowed duration of  $\text{CO}_2$  absorption is shorter than the time needed for full capacity utilization. Clearly, the current protocol, which was chosen empirically, employs an unnecessarily long capture period. In a realistic system, engineering trade-offs would be implemented to optimize the turn-around rate and energy input.

## $\text{CO}_2$ molar work calculations

The  $\text{CO}_2$  molar work of the cycles with electrochemical rebalancing,  $\bar{w}_{\text{er}}$ , is calculated as follows:

$$\bar{w}_{\text{er}} = \frac{w_{\text{cycle}}}{n \times \Phi} \times (1 + X \times (1 - \text{CE}))$$

Where  $w_{\text{cycle}}$  is the net cycle work, that is, the sum of deacidification work and acidification work;  $n$  is the number of electrons discharged;  $\Phi$  is the theoretical amount of  $\text{CO}_2$  that can be captured by a mol of hydroxide generated or electron passed, calculated according to the equations 1 through 10 in the Thermodynamic Analysis section of the previous work<sup>22</sup>;  $X$  is the ratio of the rebalancing cost to the molar cycle work and CE is Coulombic efficiency.

$\Phi$  is calculated to be 0.85 for the conditions in Supplementary Fig. 24, that is, 20% or 0.2 bar, inlet  $\text{CO}_2$  and 0.2 M hydroxide generated during electrochemical reduction of 1,8-ESP. Note that although the exit  $\text{CO}_2$  concentration is 20%, or 0.2 bar, in the experiments shown in Supplementary Fig. 24, in the calculation, it is assumed to be 100%, or 1 bar, because such condition is closer to a realistic system. Under the experimental condition in Supplementary Fig. 24, which is 20%  $\text{CO}_2$ , or 0.2 bar, in the inlet atmosphere, 0.2 M hydroxide was generated during electrochemical reduction of 0.1 M 1,8-ESP and 100%  $\text{CO}_2$ , or 1 bar, in the exit atmosphere. The corresponding value of  $\Phi$  is 0.85. Previous experimentation on another phenazine-ferrocyanide system revealed that  $X = 1.4$  when electrochemical rebalancing is applied to a complete-out-of-balance cell, that is, when all polysolite is in the oxidized form.

## Theoretical studies

All density functional theory<sup>50</sup> (DFT) calculations were performed with the Gaussian 16. Optimized geometries, evaluated a single-point calculation and vibrational analysis of oxidized and reduced molecule at the b3lyp-D3 (ref. 51)/6-311+g(d,p) (refs. 52,53) level of theory in a polarization continuum model implicit solvent using Bondi atomic radii<sup>54</sup>. The method of optimization geometries and single-point calculation of the energy of isomerization is the same as the reduction-potential calculation. The solubility was calculated by the difference between the energy of gas phase and solution phase by using the solvation model density (SMD) model in the self-consistent reaction field at M05-2X/6-31 G<sup>55</sup> level of theory.

## Data availability

All data generated or analysed during this study are included in the published article and its Supplementary Information file. Source data are provided with this paper.

## References

1. National Centers for Environmental Information *State of the Climate: Global Climate Report for 2021* (NOAA, 2021).
2. *Negative Emissions Technologies and Reliable Sequestration: A Research Agenda* (National Academies Press, 2019).
3. Raupach, M. R. et al. Global and regional drivers of accelerating CO<sub>2</sub> emissions. *Proc. Natl Acad. Sci. USA* **104**, 10288–10293 (2007).
4. Pacala, S. & Socolow, R. Stabilization wedges: solving the climate problem for the next 50 years with current technologies. *Science* **305**, 968–972 (2004).
5. Wang, Y., Zhao, L., Otto, A., Robinius, M. & Stolten, D. A review of post-combustion CO<sub>2</sub> capture technologies from coal-fired power plants. *Energy Proc.* **114**, 650–665 (2017).
6. About CCUS (IEA, 2021); <https://www.iea.org/reports/about-ccus>
7. *Global Status of CCS 2022* (Global CCS Institute, 2022); <https://www.globalccsinstitute.com/resources/global-status-of-ccs-2022/>
8. Keith, D. W. Why capture CO<sub>2</sub> from the atmosphere? *Science* **325**, 1654–1655 (2009).
9. Shi, X. et al. Sorbents for the direct capture of CO<sub>2</sub> from ambient air. *Angew. Chem. Int. Ed.* **59**, 6984–7006 (2020).
10. IPCC *Special Report on Global Warming of 1.5 °C* (eds Masson-Delmotte, V. et al.) (WMO, 2018).
11. Rochelle, G. T. Amine scrubbing for CO<sub>2</sub> capture. *Science* **325**, 1652–1654 (2009).
12. Luis, P. Use of monoethanolamine (MEA) for CO<sub>2</sub> capture in a global scenario: consequences and alternatives. *Desalination* **380**, 93–99 (2016).
13. Keith, D. W., Holmes, G., St. Angelo, D. & Heidel, K. A process for capturing CO<sub>2</sub> from the atmosphere. *Joule* **2**, 1573–1594 (2018).
14. Rinberg, A., Bergman, A. M., Schrag, D. P. & Aziz, M. J. Alkalinity concentration swing for direct air capture of carbon dioxide. *ChemSusChem* **14**, 4439–4453 (2021).
15. Sanz-Pérez, E. S., Murdock, C. R., Didas, S. A. & Jones, C. W. Direct capture of CO<sub>2</sub> from ambient air. *Chem. Rev.* **116**, 11840–11876 (2016).
16. McQueen, N. et al. A review of direct air capture (DAC): scaling up commercial technologies and innovating for the future. *Prog. Energy* **3**, 032001 (2021).
17. Kang, J. S., Kim, S. & Hatton, T. A. Redox-responsive sorbents and mediators for electrochemically based CO<sub>2</sub> capture. *Curr. Opin. Green Sustain. Chem.* **31**, 100504 (2021).
18. Muroyama, A. P., Pătru, A. & Gubler, L. Review—CO<sub>2</sub> separation and transport via electrochemical methods. *J. Electrochem. Soc.* **167**, 133504 (2020).
19. de Lannoy, C.-F. et al. Indirect ocean capture of atmospheric CO<sub>2</sub>: part I. Prototype of a negative emissions technology. *Int. J. Greenhouse Gas Control* **70**, 243–253 (2018).
20. Rheinhardt, J. H., Singh, P., Tarakeshwar, P. & Buttry, D. A. Electrochemical capture and release of carbon dioxide. *ACS Energy Lett.* **2**, 454–461 (2017).
21. Sharifian, R., Wagterveld, R. M., Digdaya, I. A., Xiang, C. & Vermaas, D. A. Electrochemical carbon dioxide capture to close the carbon cycle. *Energy Environ. Sci.* **14**, 781–814 (2021).
22. Jin, S., Wu, M., Gordon, R. G., Aziz, M. J. & Kwabi, D. G. pH swing cycle for CO<sub>2</sub> capture electrochemically driven through proton-coupled electron transfer. *Energy Environ. Sci.* **13**, 3706–3722 (2020).
23. Jin, S., Wu, M., Jing, Y., Gordon, R. G. & Aziz, M. J. Low energy carbon capture via electrochemically induced pH swing with electrochemical rebalancing. *Nat. Commun.* **13**, 2140 (2022).
24. Huang, C. et al. CO<sub>2</sub> capture from flue gas using an electrochemically reversible hydroquinone/quinone solution. *Energy Fuels* **33**, 3380–3389 (2019).
25. Xie, H. et al. Low-energy-consumption electrochemical CO<sub>2</sub> capture driven by biomimetic phenazine derivatives redox medium. *Appl. Energy* **259**, 114119 (2020).
26. Xie, H. et al. Low-energy electrochemical carbon dioxide capture based on a biological redox proton carrier. *Cell Rep. Phys. Sci.* **1**, 100046 (2020).
27. Kwabi, D. G., Ji, Y. L. & Aziz, M. J. Electrolyte lifetime in aqueous organic redox flow batteries: a critical review. *Chem. Rev.* **120**, 6467–6489 (2020).
28. Voskian, S. & Hatton, T. A. Faradaic electro-swing reactive adsorption for CO<sub>2</sub> capture. *Energy Environ. Sci.* **12**, 3530–3547 (2019).
29. Rahimi, M. et al. An electrochemically mediated amine regeneration process with a mixed absorbent for postcombustion CO<sub>2</sub> capture. *Environ. Sci. Technol.* **54**, 8999–9007 (2020).
30. Salles, M. B. C., Gadotti, T. N., Aziz, M. J. & Hogan, W. W. Potential revenue and breakeven of energy storage systems in PJM energy markets. *Environ. Sci. Pollut. Res.* **28**, 12357–12368 (2021).
31. Kwabi, D. G. et al. Alkaline quinone flow battery with long lifetime at pH 12. *Joule* **2**, 1894–1906 (2018).
32. Jin, S. et al. Near neutral pH redox flow battery with low permeability and long-lifetime phosphonated viologen active species. *Adv. Energy Mater.* **10**, 2000100 (2020).
33. Tiwari, S. P. et al. Foaming dependence on the interface affinities of surfactant-like molecules. *Ind. Eng. Chem. Res.* **58**, 19877–19889 (2019).
34. Diederichsen, K. M., Liu, Y., Ozbek, N., Seo, H. & Hatton, T. A. Toward solvent-free continuous-flow electrochemically mediated carbon capture with high-concentration liquid quinone chemistry. *Joule* **6**, 221–239 (2022).
35. Goto, K., Kodama, S., Higashii, T. & Kitamura, H. Evaluation of amine-based solvent for post-combustion capture of carbon dioxide. *J. Chem. Eng. Jpn* **47**, 663–665 (2014).
36. House, K. Z., Harvey, C. F., Aziz, M. J. & Schrag, D. P. The energy penalty of post-combustion CO<sub>2</sub> capture & storage and its implications for retrofitting the U.S. installed base. *Energy Environ. Sci.* **2**, 193–205 (2009).
37. Hitchcock, L. B. Rate of absorption of carbon dioxide effect of concentration and viscosity of caustic solutions. *Ind. Eng. Chem.* **26**, 1158–1167 (1934).
38. Hu, G. et al. Carbon dioxide absorption into promoted potassium carbonate solutions: a review. *Int. J. Greenhouse Gas Control* **53**, 28–40 (2016).
39. Pinsent, B. R. W., Pearson, L. & Roughton, F. J. W. The kinetics of combination of carbon dioxide with hydroxide ions. *Trans. Faraday Soc.* **52**, 1512–1520 (1956).
40. Ji, Y. et al. A phosphonate-functionalized quinone redox flow battery at near-neutral pH with record capacity retention rate. *Adv. Energy Mater.* **9**, 1900039 (2019).
41. Pang, S., Wang, X., Wang, P. & Ji, Y. Biomimetic amino acid functionalized phenazine flow batteries with long lifetime at near-neutral pH. *Angew. Chem. Int. Ed.* **60**, 5289–5298 (2021).
42. Xu, J., Pang, S., Wang, X., Wang, P. & Ji, Y. Ultrastable aqueous phenazine flow batteries with high capacity operated at elevated temperatures. *Joule* **5**, 2437–2449 (2021).
43. Liu, Y., Ye, H.-Z., Diederichsen, K. M., Van Voorhis, T. & Hatton, T. A. Electrochemically mediated carbon dioxide separation with quinone chemistry in salt-concentrated aqueous media. *Nat. Commun.* **11**, 2278 (2020).
44. Dell'Amico, L., Bonchio, M. & Companyó, X. Recent Advances in Electrochemical Carboxylation of Organic Compounds for CO<sub>2</sub> Valorization. In *CO<sub>2</sub> as a Building Block in Organic Synthesis* 225–252 (2020). (ed Shoubhik Das) (WILEY-VCH, 2020)
45. Li, X., Zhao, X. H., Liu, Y. Y., Hatton, T. A. & Liu, Y. Y. Redox-tunable Lewis bases for electrochemical carbon dioxide capture. *Nat. Energy* **7**, 1065–1075 (2022).

46. Xie, W. et al. Fundamental salt and water transport properties in directly copolymerized disulfonated poly(arylene ether sulfone) random copolymers. *Polymer* **52**, 2032–2043 (2011).
47. Beh, E. S. et al. A neutral pH aqueous organic–organometallic redox flow battery with extremely high capacity retention. *ACS Energy Lett.* **2**, 639–644 (2017).
48. Treimer, S., Tang, A. & Johnson, D. C. A consideration of the application of Koutecký–Levich plots in the diagnoses of charge-transfer mechanisms at rotated disk electrodes. *Electroanalysis* **14**, 165–171 (2002).
49. Sakai, M. & Ohnaka, N. Kinetics of the second charge transfer step in an ee mechanism by rotating ring-disk electrode voltammetry. *J. Electrochem. Soc.* **137**, 576–579 (1990).
50. Becke, A. D. Density-functional thermochemistry. III. The role of exact exchange. *J. Chem. Phys.* **98**, 5648–5652 (1993).
51. Grimme, S., Antony, J., Ehrlich, S. & Krieg, H. A consistent and accurate ab initio parametrization of density functional dispersion correction (DFT-D) for the 94 elements H–Pu. *J. Chem. Phys.* **132**, 154104 (2010).
52. Clark, T., Chandrasekhar, J., Spitznagel, G. W. & Schleyer, P. V. R. Efficient diffuse function-augmented basis sets for anion calculations. III. The 3–21+G basis set for first-row elements, Li–F. *J. Comput. Chem.* **4**, 294–301 (1983).
53. Francl, M. M. et al. Self-consistent molecular orbital methods. XXIII. A polarization-type basis set for second-row elements. *J. Chem. Phys.* **77**, 3654–3665 (1982).
54. van der Bondi, A. Waals volumes and radii. *J. Phys. Chem.* **68**, 441–451 (1964).
55. Ho, J., Klamt, A. & Coote, M. L. Comment on the correct use of continuum solvent models. *J. Phys. Chem. A* **114**, 13442–13444 (2010).
56. Savitzky, A. & Golay, M. J. E. Smoothing and differentiation of data by simplified least squares procedures. *Anal. Chem.* **36**, 1627–1639 (1964).

## Acknowledgements

Financial support received from the National Natural Science Foundation of China (22005249, 22101064) and Zhejiang Leading Innovative and Entrepreneur Team Introduction Program (2020R01004) is gratefully acknowledged. Research at Harvard University was supported by the Harvard University Climate Change Solutions Fund. We thank the Instrumentation and Service Center for

Molecular Sciences (ISCMS) and HPC Center at Westlake University for the facility support and technical assistance. We thank D.P. Schrag, T. George, A. Rinberg, Y. Jing and A. Bergman for helpful discussions. We thank X. Lu, X. Shi, Y. Chen and K. Wang for data collection and helpful discussions.

## Author contributions

P.W., Y.J., R.G.G. and M.J.A. formulated and supervised the project. S.P. and F.Y. synthesized the compounds. S.J., M.A. and D.X. performed the CO<sub>2</sub> capture tests. S.P. performed the cell cycling tests. L.L. performed theoretical analysis. S.J., P.W., Y.J. and M.J.A. wrote the paper, and all authors contributed to revising the paper.

## Competing interests

The authors declare no competing interests.

## Additional information

**Supplementary information** The online version contains supplementary material available at

<https://doi.org/10.1038/s41560-023-01347-z>.

**Correspondence and requests for materials** should be addressed to Pan Wang, Michael J. Aziz or Yunlong Ji.

**Peer review information** *Nature Energy* thanks Yayuan Liu, Shrihari Sankarasubramanian and the other, anonymous, reviewer(s) for their contribution to the peer review of this work.

**Reprints and permissions information** is available at [www.nature.com/reprints](http://www.nature.com/reprints).

**Publisher's note** Springer Nature remains neutral with regard to jurisdictional claims in published maps and institutional affiliations.

Springer Nature or its licensor (e.g. a society or other partner) holds exclusive rights to this article under a publishing agreement with the author(s) or other rightsholder(s); author self-archiving of the accepted manuscript version of this article is solely governed by the terms of such publishing agreement and applicable law.

© The Author(s), under exclusive licence to Springer Nature Limited 2023